THE UNIVERSITY OF

WARWICK

High resolution digital holographic synthetic aperture applied to deformation measurement and extended depth of field method

Daniel Claus

Optical Engineering Laboratory, School of Engineering, University of Warwick,
CV4 7AL, Coventry, UK (daniel.claus@gmx.net)

This paper discusses the potential of the synthetic-aperture method in digital holography to increase the resolution, to perform high accuracy deformation measurement, and to obtain a three-dimensional topology map. The synthetic aperture method is realized by moving the camera with a motorized x–y stage. In this way a greater sensor area can be obtained resulting in a larger numerical aperture (NA). A larger NA enables a more detailed reconstruction combined with a smaller depth of field. The depth of field can be increased by applying the extended depth of field method, which yields an in-focus reconstruction of all longitudinal object regions. Moreover, a topology map of the object can be obtained.   © 2010 Optical Society of America

OCIS codes: 090.1995, 100.2980.

1. Introduction

In digital holography the sinusoidal interference pattern resulting from the interference between reference and object wave is stored on a digital receiver, such as charged coupled device (CCD) or complementary metal oxide semiconductor (CMOS) cameras. The size of the full sensor of digital receivers is small compared to photographic plates used in optical holography. Therefore, the numerically reconstructed hologram possesses a larger speckle size, and the smallest resolvable object detail according to Abbé's criterion is larger than in optical holography. One way to improve the resolution in digital holography is the synthetic aperture method. Holograms at different lateral positions are recorded. These holograms are then stitched together to a single synthetic aperture hologram. In that manner the *space–bandwidth product* (SBP) and the numerical aperture of the hologram are increased, which results in a more detailed reconstruction. The implementation of the synthetic aperture method in digital holography has been reported by [1–10]. In most cases a spherical reference wave is chosen [3–8,10]. A spherical reference wave enables the recording of lensless Fourier holograms. Lensless Fourier holograms are obtained by locating the origin of the spherical reference wave and the object at the same distance to the camera. The minimum recording distance at which the Fourier hologram is not undersampled is

$$d_{\min} \geq \frac{2\Delta x' b}{\lambda},\qquad(1)$$

with b the distance between reference-wave source point and furthest distant object point. The nomenclature used in Eq. (1) and in the further proceeding of this paper is shown in Fig. 1. From Eq. (1) it follows that the minimum recording distance $d_{\min}$ does not depend on the pixel number. Hence the recording arrangement of Fourier holograms is perfectly suited for the synthetic aperture method. In most cases found in the literature the setup was arranged in an off-line fashion [3,5,6], which results in a separation of image, twin image, and DC term in the reconstruction and enables dynamic measurements. Other sources report an on-line setup that enables a more
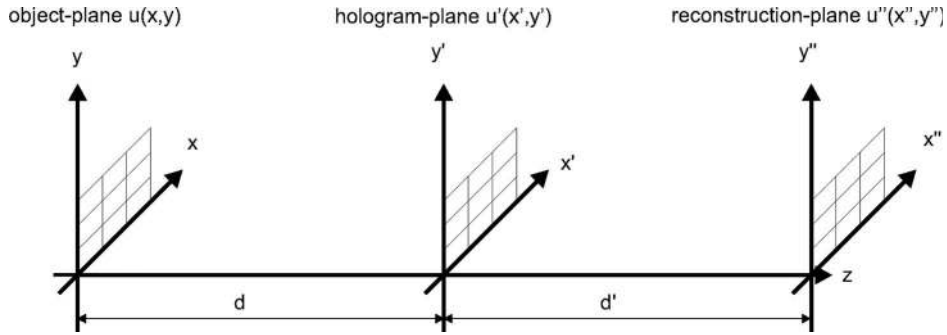
Fig. 1. Nomenclature for coordinates in the object plane, hologram plane, and reconstruction plane.

effective use of the sensor's SBP. Reference [11] reports that the SBP required for the recording is four times bigger for the off-line case than it is for the on-line. The problem arising from the on-line setup is the overlap of the twin image, the DC term, and the desired image in the numerical reconstruction. This problem can be overcome by applying phase stepping, which results in a DC term and twin image free numerical reconstruction. Phase stepping in conjunction with the synthetic aperture method was successfully demonstrated by [7] using a four-bucket phase stepping algorithm. The numerical reconstruction of Fourier holograms is similar to the reconstruction procedure of Fresnel holograms:

$$u''(x'',y'') = \frac{i \exp(ikd')}{\lambda d'} \exp\left[\frac{i\pi}{\lambda d'}(x''^2 - y''^2)\right]$$
$$\cdot \mathcal{F}\left\{u'(x',y')u_r^*(x',y')\right.$$
$$\left.\cdot \exp\left[i\frac{\pi}{\lambda d'}(x'^2 + y'^2)\right]\right\}, \quad (2)$$

where u_r^* indicates the complex conjugated reference wave. The chirp function used in the Fresnel method, which acts like a lens of focal length $f = -d'$, is already embedded in the hologram due to the spherical reference wave u_r. The spherical reference wave in the hologram plane ($d_r = d'$) can be described by

$$u_r(x',y') \approx \exp\left[i\frac{\pi}{\lambda d'}(x'^2 + y'^2)\right]. \quad (3)$$

Substituting Eq. (3) into Eq. (2) permits the elimination of the parabolic chirp function, dependent on x' and y'. Hence the reconstruction algorithm for Fourier holograms becomes

$$u''(x'',y'') = \frac{i \exp(ikd')}{\lambda d'} \exp\left[\frac{i\pi}{\lambda d'}(x''^2 - y''^2)\right]$$
$$\cdot \mathcal{F}\{u(x',y')\}. \quad (4)$$

The numerical reconstruction requires only a two-dimensional Fourier transformation of the hologram $u(x',y')$ multiplied with a phase factor; see Eq. (4). The constant phase term ($[i \exp(ikd')]/\lambda d'$) can be ne-

glected in the reconstruction process since it introduces a constant phase term. The obtained reconstructed hologram is focused at the reference-plane distance. The computationally inexpensive algorithm is offset by the inability to focus at different axial sections within the object volume, since Eq. (4) is not a function of the reconstruction distance d', as discussed in [12]. One possible way to focus at different axial object sections is to apply Eq. (2). The disadvantage of this approach is that the numerical chirp function possesses high frequencies at its edges, which might not be resolved when applying the synthetic aperture method. In order to avoid numerical undersampling the camera–object distance needs to be increased the larger the synthetic aperture becomes. Moreover, a chirp function needs to be calculated twice, once for the object wave and another time for the reference wave. A way to overcome this problem is to combine both chirp functions by which a numerical lens is created, Eq. (5), as proposed by [13,14],

$$L(x',y',d_r,d_o) = \exp\left[\frac{i\pi}{\lambda}\frac{d_r - d_o}{d_r d_o}(x'^2 + y'^2)\right]. \quad (5)$$

The numerical lens represented in Eq. (5) is a function of the reference source point distance d_r and the object distance d_o. It is convex for $d_o < d_r$ and concave for $d_o > d_r$. It possesses a very low frequent chirp function since d_r and d_o are almost matched. It can therefore be applied at any distance without the risk of undersampling or exceeding the validity of the Fresnel approximation. In general CCD cameras are used for the recording of digital holograms because their fill factor is almost 100%, and the readout is reasonably homogeneous. However, CCD technology is more expensive than CMOS. Moreover, the minimum pixel size, which determines the minimum object–camera distance, is larger for CCD cameras (3.5 μm Sony ICX625) compared to CMOS cameras (1.4 μm Aptina MT9E013). These properties support the idea to introduce CMOS technology in digital holography. The noisier readout of CMOS cameras can be reduced by hot-pixel elimination and dark field calibration prior to the measurement. In the further proceeding of this paper the increase of resolution and accuracy arising from the synthetic aperture

method, which was carried out with CMOS technology, is demonstrated.

2. Methodology

The synthetic aperture method presented in this paper was performed with a lensless 6.6 Mpixel CMOS camera (C-Cam, BCi4-6600) with 3.5 μm pixel size and 35% fill factor. In order to obtain an increased sensor area the camera is shifted by a motorized PI M150.11 x–y stage with a linear resolution of 8.5 nm. The total shift is in the range of the sensor dimension with a small overlap of approximately 200 pixels between adjacent holograms to enable accurate pixel alignment by means of cross-correlation, described by [6,7]. The setup used is shown in Fig. 2. Vertically polarized laser light from a He–Ne laser is rotated by a half-wave plate. The combination with a polarizing beam splitter cube enables the adjustment of reference-wave and object-wave *intensity*. In addition the *polarization* of both reference and object wave can be matched by placing two quarter-wave plates in the reference arm. Both intensity and polarization adjustment ensure a good contrast of the recorded interference pattern.

To demonstrate the resolution improvement the synthetic aperture method has been evaluated using the USAF 1951 test target. A parameter to define the resolution and imaging performance improvement of the reconstructed holograms is the SBP. The SBP of the reconstructed hologram represents the product of the field of view (FOV) and the highest resolvable spatial frequency. The calculation of the SBP was taken from [15]

$$\mathrm{SBP} = \delta_{x''}^{-1} \cdot \delta_{y''}^{-1} \cdot N\Delta x'' \cdot M\Delta y'', \tag{6}$$

where $\delta_{x''}$ and $\delta_{y''}$ are the smallest resolvable object details in horizontal and vertical direction, respectively, and the product $N\Delta x'' \cdot M\Delta y''$ is the FOV of the numerical reconstruction. In this particular case N and M denote the number of pixels that display the reconstructed image. The SBP is a more meaningful parameter than the resolution itself for the judgment of optical systems since it is independent from the recording distance and permits the comparison of different optical systems. The optimum SBP for Fourier holograms can be calculated with the help of Eq. (1). An on-line setup is assumed, which means that b from Eq. (1) becomes half the largest object dimension (O). Thus the FOV corresponds to

$$\mathrm{FOV} = O \cdot O. \tag{7}$$

The smallest resolvable object detail for x'' and y'' becomes

$$\delta_{x''} = \frac{O}{N} \quad \text{and} \quad \delta_{y''} = \frac{O}{M}. \tag{8}$$

Thus the optimum SBP for on-line Fourier holograms is

$$\mathrm{SBP}_{\text{on-line}} = N \cdot M. \tag{9}$$

In the case of an off-line setup the SBP is

$$\mathrm{SBP} = \frac{N \cdot M}{4}. \tag{10}$$

In conclusion, the on-line setup has a SBP for the reconstructed hologram that is four times larger than in the off-line case, which is in accordance with [15]. In order to measure the setup performance with respect to its optimum SBP an efficiency parameter η is introduced:

$$\eta = \frac{\mathrm{SBP}}{\mathrm{SBP}_{\text{on-line}}} \cdot 100\%. \tag{11}$$

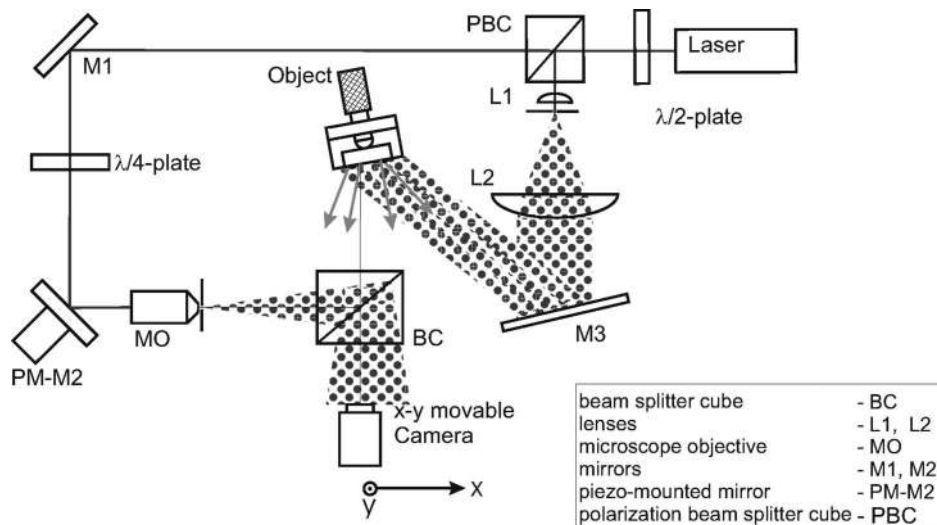In this manner different optical setups can be compared.

Fig. 2. Sketch of setup for recording a Fourier hologram.

A suitable parameter to describe image quality improvement for intensity and double-exposure phase maps is the signal-to-noise ratio (SNR). SNR can be calculated according to [16] by

$$\mathrm{SNR} = 20\log\left(\frac{\bar{X}}{\sigma}\right), \qquad (12)$$

where $\bar{X}$ is the mean value of a population and σ the standard deviation. Assuming that the noise is evenly distributed over the reconstruction, only a small region of interest of approximately 200×200 pixels with ideally constant gray level needs to be considered for the SNR measurement. Gray level changes in that region should then solely be due to noise. The majority of pixels of a double-exposure phase map lie within a 2π boundary. The phase gradient results in a fluctuation of phase values. This fluctuation produces an error when calculating the SNR. Therefore the SNR is determined by calculating the standard deviation along a minimum fringe gradient.

3. Resolution Improvement

The resolution improvement with the synthetic aperture method was determined utilizing the USAF 1951 test target as the object under investigation. First, a Fourier hologram without applying the synthetic aperture was recorded. Zero padding was applied to generate a hologram of equal dimensions in the x and y directions [see Fig. 3(a)]. In this manner the reconstructed hologram does not suffer from different pixel sizes $\Delta x''$ and $\Delta y''$ [Eq. (13)], which would otherwise result in a stretched reconstruction and possess different depth of field and resolution in vertical and horizontal direction:

$$\Delta x'' = \frac{\lambda d'}{N\Delta x'} \quad \text{and} \quad \Delta y'' = \frac{\lambda d'}{M\Delta y'}, \qquad (13)$$

where N and M are the pixel numbers in the x and y directions, respectively.

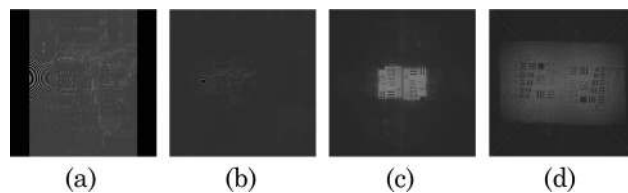Afterwards a hologram was recorded with the synthetic aperture method. Figures 3(a) and 3(b) show

Fig. 3. Hologram at recording distance of 295 mm for (a) 3000 × 3000 pixels, (b) 8000 × 8000 pixels, and their reconstructions (c) and (d), respectively.

the recorded holograms, and Figs. 3(c) and 3(d) show their reconstructions for 3000 × 3000 pixels and 8000 × 8000 pixels, respectively. In order to observe the smallest resolvable object detail a small region has been selected, shown in Fig. 4. The smallest resolvable test target element was obtained by calculating an averaged cross section for the investigated element. The cross sections are shown in Fig. 4, where the x axis denotes the pixel number and the y axis the normalized intensity. Care was taken so that the three local minima (black strips) are visible and the ratio of the largest local minima to the smallest local maxima is less than 0.75 according to the resolution criterion. The black ring in Fig. 4 encircles the horizontal resolution, and the white ring the vertical one. According to Abbé's criterion the theoretically possible resolution was calculated and compared to the obtained resolution of the reconstructed holograms; see Table 1. Three statements can be concluded from this comparison. First, the obtained resolution with the synthetic aperture method is almost three times larger than the resolution obtained with a single hologram. Second, the result obtained matches well with the expected value. Last but not least, the vertical and horizontal resolution obtained differ slightly, which might be due to different vertical and horizontal dimensions of the light-sensitive pixel area. The results obtained were then compared with recent publications [3,10]. Instead of only taking into account the smallest resolvable object detail the SBP of the reconstructed hologram was calculated.
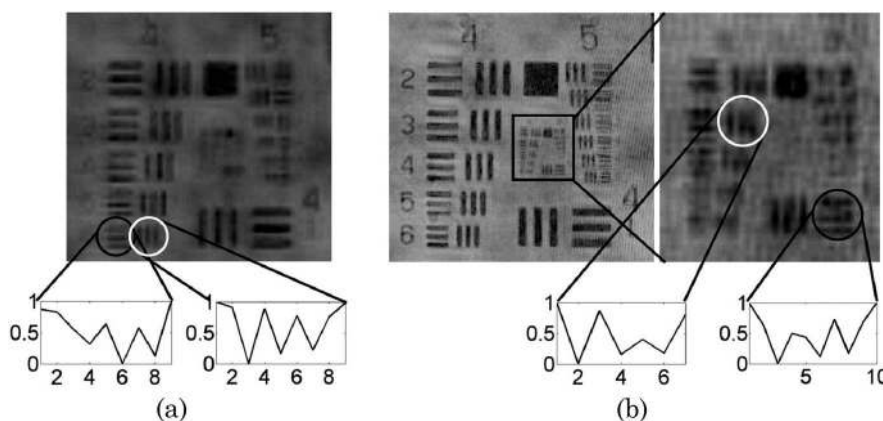

Fig. 4. Region of interest including averaged cross-section for (a) 3000 × 3000 pixel hologram, (b) 8000 × 8000 pixel hologram.

Table 2. SBP Comparison

Parameters	Own Results	Results from Ref. [3]	Results from Ref. [10]
Pixel number	8000 × 8000	5000 × 5000	5120 × 5120
Pixel size [μm]	3.5	7	7.5
FOV [mm^2]	30 × 23	4 × 4	330 × 330
$\delta_{x''}$ [μm]	7.8	2.6	446.4
$\delta_{y''}$ [μm]	6.2	2.6	446.4
SBP [10^6]	14.27	2.37	0.55
η [%]	22.3	9.5	2.1

The SBP for the reconstructed hologram obtained is more than six times larger than what is to the author's knowledge the up to date best published result. The value of η is close to the theoretical value of 25% according to Eq. (10) and is largest compared to the two cited papers; see Table 2. This is due to the recording setup and the camera used. The experiments in the two cited papers were performed with a CCD camera of bigger pixel size. Furthermore, in both papers optical imaging elements were used between object and camera, which might explain the lower η. The result could prove that CMOS cameras can perform at least equally well as CCD cameras under sufficient lighting conditions.

4. Deformation Measurement

The object under investigation is a cantilever. Attached to the cantilever is a micrometer screw, which permits the application of a precise deformation to the cantilever. The setup used is shown in Fig. 2. The object–camera distance is 780 mm and the mirror illuminating the object is laterally displaced from the object–camera axis by 260 mm. The camera has been moved in a 4 × 3 grid to 12 different positions. The generated synthetic aperture hologram occupied a
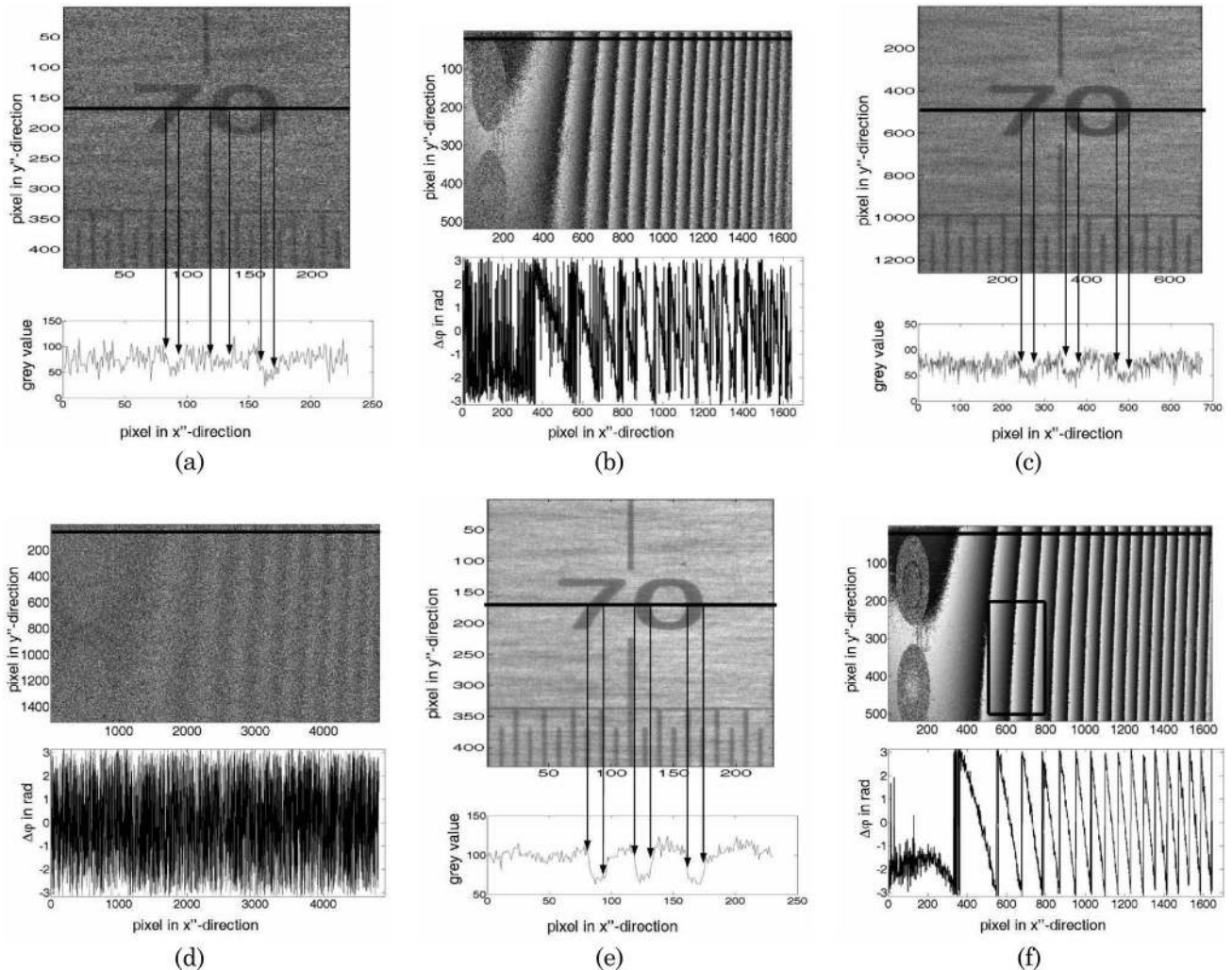

Fig. 5. Segment of reconstructed intensity and double-exposure phase map including cross-section (a), (b) 3000 × 3000 pixels, (c), (d) 8800 × 8800 pixels, and (e), (f) 3000 × 3000 pixel averaging approach.

sensor area of 8800×8800 pixels. The results obtained for the intensity reconstruction of the cantilever is shown in Fig. 5(c). It demonstrates an increase in SNR from 24.06 dB for a reconstructed 3000×3000 pixel hologram to 26.66 dB for a reconstructed 8800×8800 pixel synthetic aperture hologram.

The synthetic aperture method was applied to digital double-exposure holography by moving the camera to a sequence of positions for the *unloaded object* state and then repeating the sequence again exactly for the same positions for the *loaded object* state. A synthetic aperture hologram was obtained for both object states. Both synthetic aperture holograms were aligned to each other utilizing cross-correlation and then numerically reconstructed. The change of angle between the illumination and observation vector for the centered and most displaced position is 0.2°. Thus the influence on the sensitivity vector and the corresponding phase shift in the double-exposure phase map is negligible. The double-exposure phase map was calculated by subtracting the reconstructed phase of the loaded state φ_2 and the unloaded state φ_1 Eq. (14):

$$\Delta\varphi(x'', y'') = \varphi_2(x'', y'') - \varphi_1(x'', y''). \quad (14)$$

The resulting double-exposure phase map, shown in Fig. 5(d), is less well defined. The phase contrast of the 2π phase jumps is reduced, which might be due to alignment errors. It was noticed when illuminating the sensor with a collimated laser beam that the sensor possesses a slight curvature. Figure 6(a) shows the diffraction pattern obtained from the sensor. The diffraction pattern for an optimum flat sensor should be orientated along straight lines. In our case parabolic lines were obtained that are evidence of a convex sensor curvature. This results in scanning at different axial positions of the incoming speckle field [see Fig. 6(b)] and hence introduces alignment errors.

In addition, the reliability of the cross-correlation values obtained have been examined by calculating its standard deviation. The shift amount in the horizontal direction is 1972 ± 0.795 pixels and in the vertical direction 2781 ± 1.609 pixels. The larger residual in the vertical direction might be due to a larger shift applied, which is combined with an increased axial speckle decorrelation. The error represented in this case is a combination of cross-correlation error and lateral alignment error arising from the x–y stage. Three additional alignment errors between adjacent holograms and hologram pairs, which represent the two laterally corresponding holograms for the unloaded and loaded object state, could be defined. In conclusion, possible alignment errors might have arisen from

   i.   cross-correlation error,
   ii.   cross-correlation detected lateral misalignment between adjacent holograms and hence laterally corrected,
   iii.   axial misalignment between adjacent holograms,
   iv.   axial misalignment between corresponding hologram pairs,
   v.   lateral misalignment between corresponding hologram pairs.

The consequences of these errors on lateral and axial alignment are shown in Table 3, where 0 indicates no impact and 1 indicates that an impact occurred. This consideration assumes that each error possesses the same degree of impact.

A curved sensor is more than twice as sensitive to pick up axial alignment errors than a plane sensor is, according to Table 3. Moreover, the impact of axial misalignment is amplified due to the optical setup's sensitivity for out of plane (axial) phase changes. If the two unloaded and loaded holograms at position P_k differ in their axial alignment a constant phase offset is introduced in the resulting double-exposure phase map, shown in Fig. 6(c). Consequently, each of the laterally corresponding hologram pairs might have a different phase offset. Thus combining the information of all hologram pairs to a synthetic aperture hologram results in a double-exposure phase map of low phase contrast, as shown in Fig. 5(d). Possible ways to avoid the introduction of a phase offset between hologram pairs are

• to use a plane sensor, which is less sensitive at picking up axial misalignment errors (see Table 3),
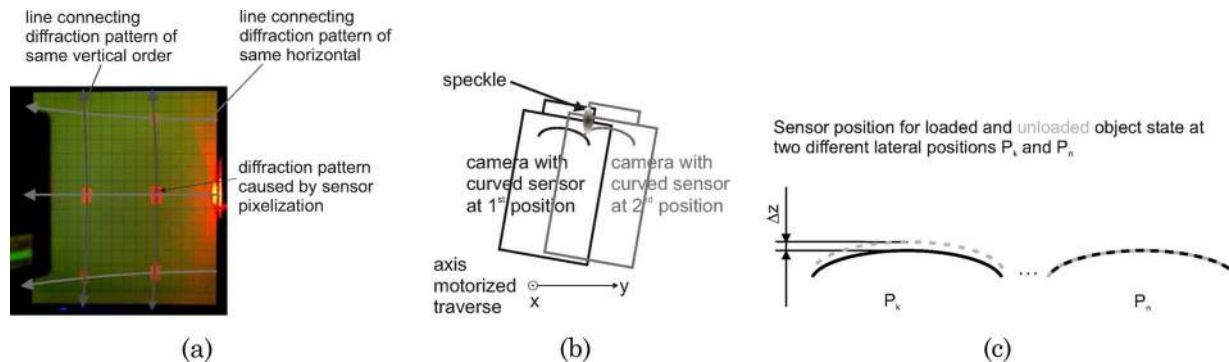

Fig. 6. (Color online) (a) Diffraction caused by collimated illumination of the sensor, (b) sketch of the axial speckle decorrelation due to camera and/or curved sensor, (c) phase offset caused by axial displacement between the two double-exposure camera positions.

Table 3. Consequences on Lateral and Axial Alignment

Error	Lateral Alignment	Axial Alignment (Curved Sensor)	Axial Alignment (Plane Sensor)
i	1	1	0
ii	0	1	0
iii	0	1	1
iv	0	1	1
v	1	1	1
$\sum$	2	5	2

- to record all laterally shifted holograms simultaneously at fixed positions utilizing a camera array,
- to apply phase stepping digital holography, which enables the elimination of the phase offset between adjacent holograms prior to the reconstruction process,
- to apply *spatial averaging* as described in [5].

The original spatial averaging approach was slightly modified and used in this paper to overcome the problem of low phase contrast. Its flow chart is shown in Fig. 7. The loaded object state in Fig. 7 is denoted by $\tilde{u}'$ for the recorded hologram and $\tilde{u}''$ for its numerical reconstruction. Moreover, the functions medfilt2 and angle indicate Matlab functions that are used to median filter the image and to calculate the phase of the complex exponential reconstruction, respectively. The spatial averaging approach is realized by reconstruction of each individual hologram using Eq. (4). Due to the shift $\delta x'$ and $\delta y'$ in the hologram plane the reconstructed hologram needs to be

multiplied with an additional complex exponential phase factor:

$$\delta\varphi(x'',y'') = i\frac{2\pi}{\lambda d}(x''\delta x' + y''\delta y').\qquad(15)$$

The additional phase term affects only the phase and does not need to be applied to average intensity reconstructions. Furthermore, it can be eliminated for double-exposure holograms since it is of same magnitude and sign for both deformation states. The averaged double-exposure hologram is obtained by calculating the individual double-exposure holograms at each position. In that manner a phase offset can be removed from each individual double-exposure hologram. The phase offset is determined in an iterative manner by taking the phase map at the last position P_n as a reference phase; see Fig. 7. At this position the camera has not been traversed to other positions when recording the unloaded and loaded object state. Hence it should not have any phase offset or phase tilt due to lateral displacement. The phase offset and an eventual phase tilt is then subtracted from the phase map at the corresponding positions. In order to avoid smearing the phase maps are then added up in a complex notation; see Fig. 7. The double-exposure phase maps obtained for a single position, the synthetic aperture method, and the spatial averaging approach are shown in Figs. 5(b), 5(d), and 5(f), respectively. A significant image quality improvement between the synthetic aperture method and the spatial averaging approach is demonstrated. The SNR values were calculated for the region shown in Fig. 5(f) at the same
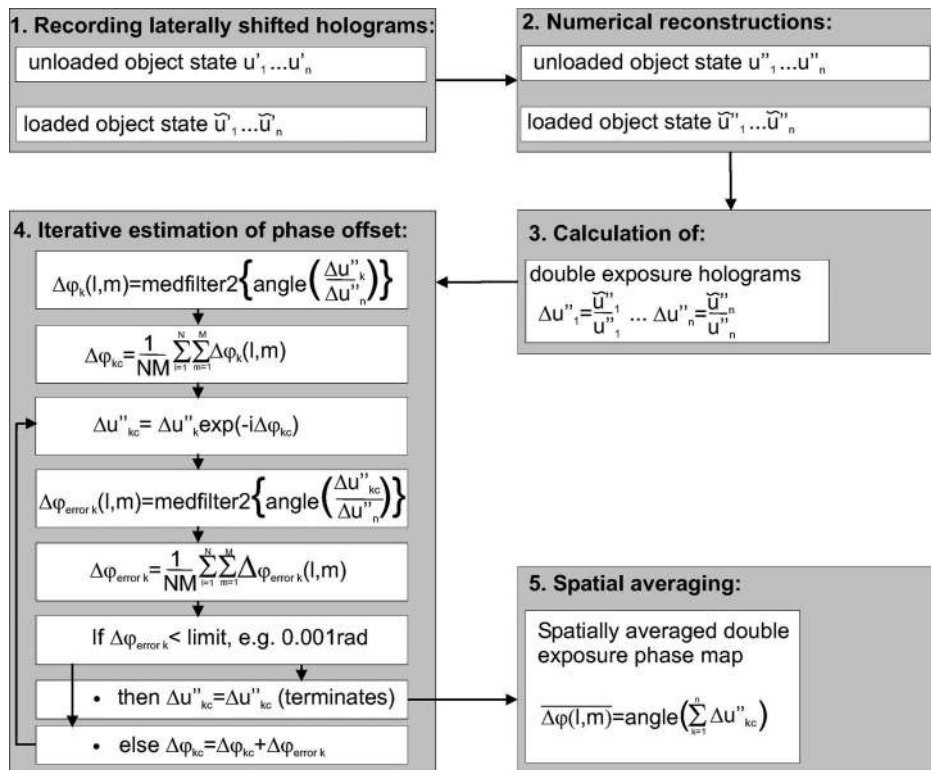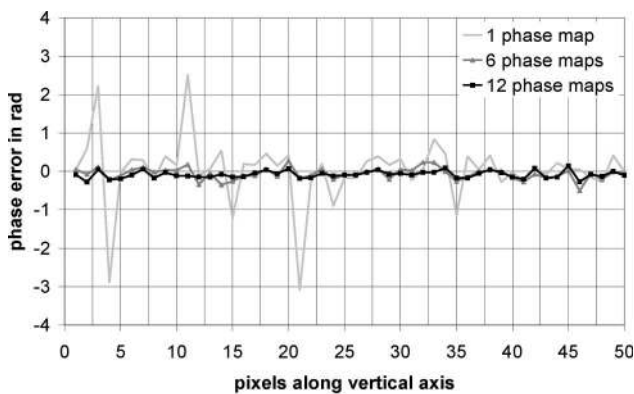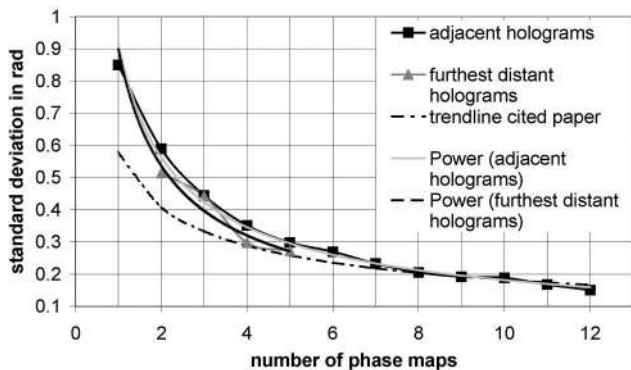

Fig. 7. Flow chart of the spatial averaging approach applied to double-exposure holography.

corresponding position for all three phase maps. The values obtained are 17.22 dB, 11.47 dB, and 25.57 dB. Thus the double-exposure phase map obtained by the spatial averaging approach possesses a higher accuracy, which can be shown by the Fig. 8. The standard deviation is reduced from 0.85 rad with a single double-exposure hologram to 0.15 rad by using 12 double-exposure holograms. The relative object deformation can be calculated by taking into account the setup geometry and the resulting sensitivity vector. The obtained deformation values for each case are $\frac{\lambda}{14}$ and $\frac{\lambda}{81}$, respectively. The gradient of the standard deviation trend line shown in Fig. 8(b) is higher than the one obtained by [5]. This is due to a larger shift between the recording of the consecutive holograms. In [5] a lateral shift of 5 mm was applied, whereas in our case a vertical shift of 7 mm and a horizontal shift of 9.8 mm was applied. The higher gradient requires less holograms to be recorded in order to obtain a similar result as in [5]. Although the initial standard deviation for a single reconstruction is higher than in [5] only 12 holograms needed to be recorded instead of 25. Furthermore it can be shown that the further distant the holograms used for the spatial averaging method are the better is the result; see Fig. 8(b). The standard deviation could be approximated by a power function:

Table 4. Trend-line Standard Deviation of Phase

Parameters	Adjacent Holograms	Furthest Distant Holograms	Result Obtained by Ref.[5]
a	0.9165	0.8987	0.5773
b	−0.70	−0.74	−0.50
R^2	0.994	0.932	–

$$f(x) = ax^b. \tag{16}$$

The values of a and b are shown in Table 4. Figure 8(a) shows the deviation of the phase from the mean value along a cross section in the region under investigation; see the boxed area in Fig. 5(f). The area under investigation was rotated by 5.5° in order to scan along the fringe orientation. The averaging approach has also been applied to intensity reconstructions. Contrary to the double-exposure phase the influence of a possible phase offset is not too severe for the intensity reconstruction [see Fig. 5(c)]. Figure 5(e) shows a segment of the reconstructed intensity image with an SNR value of 36.61 dB. In Fig. 9 the SNR of the intensity reconstruction and double-exposure phase map is shown. The relationship between number of holograms used and the SNR follows to a good approximation a logarithmical curve described by

$$f(x) = a \cdot \ln(x) + b. \tag{17}$$

Fig. 8. (a) Phase error for a vertical cross-section of the area under investigation, (b) standard deviation of double-exposure phase maps for adjacent and furthest distant holograms including the trend line.
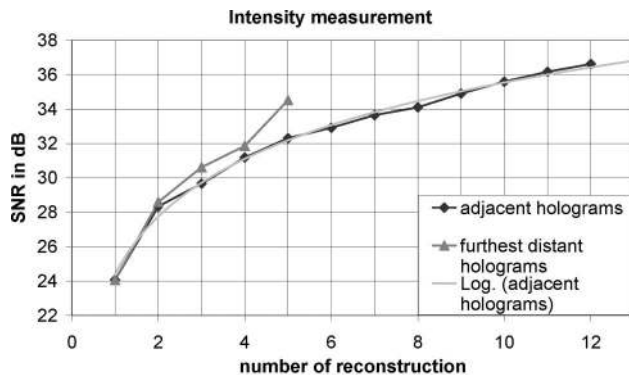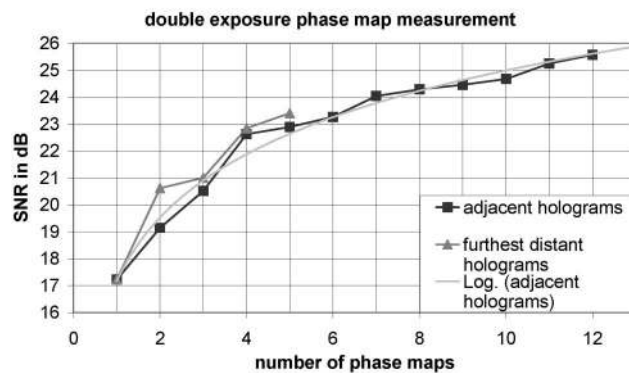

Fig. 9. (a) SNR for intensity reconstruction versus number of images and their position, (b) SNR for phase map versus number of images and their position.

Table 5. SNR Spatial Averaging Method for Intensity and Double-Exposure Phase Map

Parameters	Intensity Reconstruction	Double-Exposure Phase Map
a	4.842	3.3973
b	24.392	17.169
R^2	0.995	0.985

The logarithmical coefficients and the *squared correlation coefficient* R^2 are shown in Table 5. In conclusion, the statements previously made for the standard deviation concerning the improvement in conjunction with number of holograms used for the spatial averaging approach and the lateral displacements between holograms could be confirmed by the SNR curves.

5. Extended Depth of Field

Depth of field (DOF) describes the region along the z axis, where the object is still imaged sharply. This is the case when the circle of confusion is not larger than a single pixel in the reconstruction plane [17], which is satisfied for the region l_{df}. The equation to calculated the DOF for a Fourier hologram can be derived with the help of Fig. 10 and geometric relations

$$l_{df} = \frac{2d'N\Delta x'\Delta x''}{N^2 \Delta x'^2 - \Delta x''^2}.$$ (18)

The DOF obtained for a synthetic aperture hologram of 8800×8800 pixels is 0.7 mm. The object of investigation is the same cantilever as previously used. The advantage of a more detailed reconstruction gained by the synthetic aperture method is offset by a smaller DOF [Eq. (18)]. Only a small axial region of a three-dimensional object is sharply represented in the reconstruction plane (Fig. 11). This problem can be overcome by means of the *extended depth of field* (EDOF) method originally applied in confocal microscopy. As a result an image with all parts in focus and a topology map can be obtained. The EDOF method was already applied to digital holography in [18–20], but to the authors knowledge it is the first
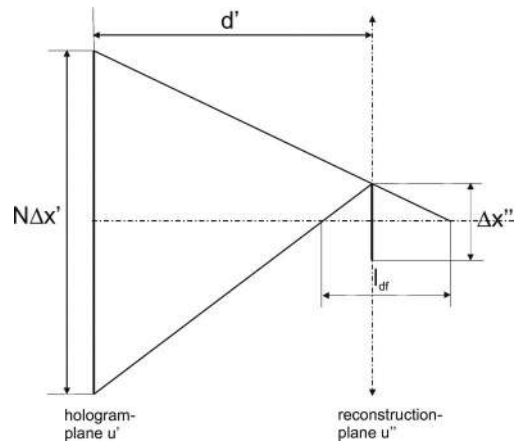

Fig. 10. Sketch of the DOF for a reconstructed hologram.

time to report the combination of synthetic aperture method with the EDOF method. Not all algorithms used in microscopy to define the in-focus object regions can successfully be applied in digital holography due to the speckle effect. The most promising algorithm is based on the variance approach, demonstrated in [19,20], which was also applied in this paper. Speckle noise apparent in the numerical reconstruction produces a large change of variance. Therefore, before calculating the variance the speckle noise needs to be reduced by applying a speckle filter, as in [19], and/or resizing the reconstructed hologram. Furthermore, the variance method requires sufficient object illumination of all parts under investigation. The object illumination ideally is homogeneous in order to obtain a good contrast of all object parts yielding in large deviation of variance values. A further requirement is to use the correct *window size* (WS) for which the variance is calculated. If the WS is too small, fine object details are reproduced in the topology map. A too large WS results in a reduced accuracy of the topology map. A last limitation of this method is that the axial resolution of the topology map depends on the numerical aperture and wavelength of the optical system. For macroscopic objects the obtainable axial resolution is only in the mm range. Having discussed the limitations the main advantage of this method needs to be put in focus.
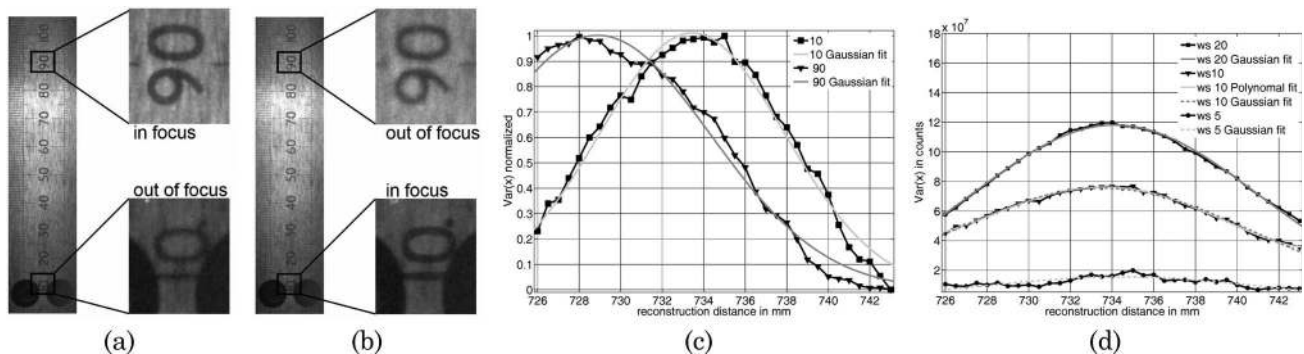

Fig. 11. (a) Intensity reconstruction for $d' = 728$ mm, (b) intensity reconstruction for $d' = 735$ mm, (c) variance plot for both boxed areas including Gaussian curve fitting, (d) Gaussian curve fitting for different WS and comparison polynomial fitting for WS of 10×10 pixels.

Instead of recording images focused at different axial positions of the object, only one hologram is numerically refocused to different axial positions. Thus the experimental effort and disturbing environmental influences are minimized. As a result a high resolution reconstruction of all parts in focus and the topology map of the object under investigation is obtained. Another possible application is the generation of a three-dimensional particle field and temporal three-dimensional particle tracking.

A. Variance Approach

The numerical focusing at different axial planes is obtained by reconstructing the hologram with help of Eq. (4) and a numerical lens described in Eq. (5). The number of reconstructions N_r required in order to obtain an image with all object parts in focus depends on the DOF and on the axial extension of the investigated object Z_{obj}:

$$N_r \geq \frac{Z_{obj}}{l_{df}}. \qquad (19)$$

The refocusing range is defined by the upper and lower limit where the reconstruction is out of focus. In our case this was between 726 mm and 743 mm reconstruction distance with 0.5 mm reconstruction step width. The reconstructed holograms were ordered in a stack according to their reconstruction distance, 726 mm top and 743 mm bottom. Some preprocessing is needed before applying the EDOF method. The region of interest was cut out and then resized to a quarter of its original size from 3600×832 pixels to 900×208 pixels. This step was necessary in order to minimize the calculation time and to reduce the impact of speckle noise on the variance measurement. The speckle size after resizing is less than the size of a pixel, as a result of which it was not necessary to apply speckle-noise reduction filters, as in [19]. The variance of each pixel was calculated with a 10×10 pixel WS. This size was experimentally found to give the best results. In order to obtain the EDOF reconstruction the stack of the calculated variance maps was binarized on a column by column basis with the threshold set at the maximum variance value in each pixel column. Afterwards, this stack was multiplied in a pixelwise manner with the stack of the reconstructed images.

A reconstruction with all parts in focus was obtained, shown in Fig. 12. The topology map was obtained by recording the position of the maximum variance value for each column in a two-dimensional map. The number of discretization levels equals the number of reconstruction planes. The topology map was then inverted to present those points that project from the flat surface of the object with a larger intensity level (see Fig. 12).

B. Gaussian Fitting

Figure 11(c) represents the variance value at each reconstruction distance for both boxed areas shown in Figs. 11(a) and 11(b). One can conclude that the variance values could be approximated by a *Gaussian curve* defined by the equation

$$f(x) = a \exp[-((x - b)/c)^2], \qquad (20)$$

where a, b, and c are the Gaussian coefficients. For both boxed regions shown in Figs. 11(a) and 11(b) the Gaussian coefficients are shown in Table 6. The R^2 values and the sharpness–distance relationship described by other authors [21] confirm the validity of the Gaussian approximation. In practice, instead of a Gaussian approximation a fourth-degree polynomial approximation was applied to obtain interpolated variance values. In this manner the calculation time could be reduced and the algorithm became more insensitive to any calculation errors, which would have caused the program to end abruptly. These errors occurred whenever the maximum variance value was close to the first or last distance value. In this case no Gaussian function could be found to fit the data. The Gaussian curve and the fourth-degree polynomial curve are shown in Fig. 11(d) for a WS of 10×10 pixels.

It can be concluded from Fig. 11(d) that the Gaussian fitting can be used to obtain the correct sliding WS to calculate the variance values. This can be achieved utilizing the R^2 values, which describes how well the measurement values matches with the Gaussian curve. The R^2 values obtained are 0.667, 0.989, and 0.997 for a WS of 5×5, 10×10,
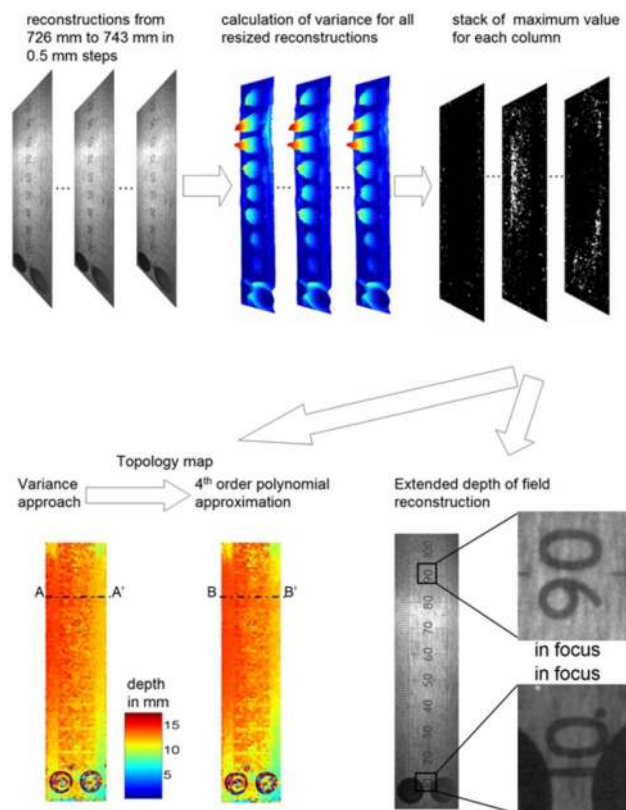

Fig. 12. (Color online) Topology map.

Table 6. Gaussian Coefficients and R^2 Values

Area under Investigation	Boxed Area 90	Boxed Area 10
a	0.9843	0.9834
b	728.1	733.5
c	11.4	10.35
R^2	0.9893	0.9893

and 20×20 pixels, respectively. Furthermore, the precision of the topology map could be improved by creating a larger amount of discretization levels. The obtained interpolated maximum value is used instead of the original maximum variance value. In this manner the number of discretization levels increased from 35 by solely applying the variance approach to 349 by applying the polynomial interpolation. This is shown in Figs. 13(a) and 13(b), respectively. Last but not least, location errors for the maximum variance value as shown in Fig. 11(c) can be reduced by the interpolated maximum value, which results in an accuracy improvement of the topology map. This could be demonstrated by a de-
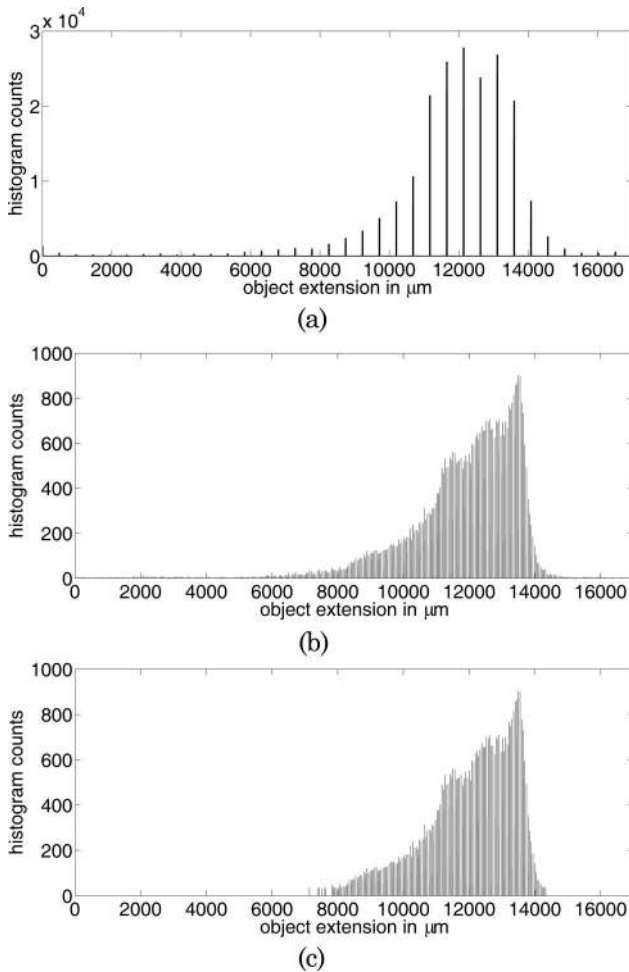

Fig. 13. Histograms for obtained topology map with (a) traditional variance approach, (b) polynomial interpolation, (c) bandpass filtered polynomial interpolation.
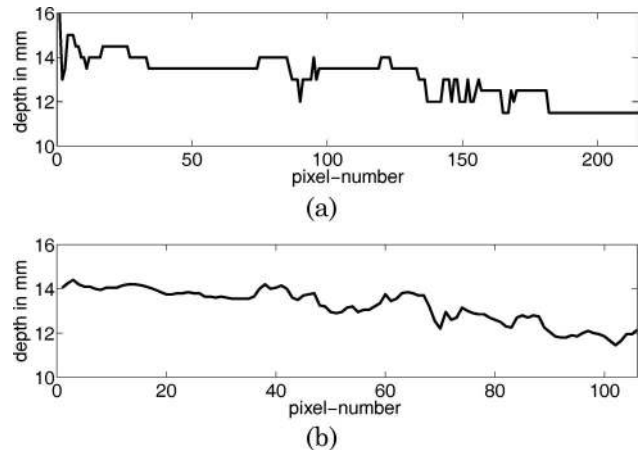

Fig. 14. Cross-sections for cut lines shown in Fig. 11, (a) A-A′, (b) B-B′.

creasing standard deviation calculated for both cross-sections shown in Fig. 14 from 0.96 mm to 0.79 mm. These advantages are offset by the long processing time. Despite the reduction of the stack size from $35 \times 342 \times 1100$ pixels to $35 \times 171 \times 550$ pixels the calculation time was 40 min with a server using an Intel Xeon at 2 GHz processor on Matlab at 64 bits. In comparison, the previously described variance approach applied to the original stack size needed, 57 s.

The axial extension obtained from the topology map for the cantilever is 7.14 mm, as shown in Fig. 12 and in the noise-filtered histogram, Fig. 13(c). To validate the holographically obtained topology data a tactile method using a Vernier caliper was applied. The axial length differences between the deflected cantilever to its mount was measured at its four corners. The cantilever was tilted, producing an axial displacement of 5 mm in the vertical direction. Furthermore, it was positioned with a slight angle to the camera in the horizontal plane, producing a further axial displacement of 2 mm. Thus the obtained result for the topology map could be confirmed by the measured values with an accuracy to the order of a millimeter. Further calibration work is required in order to validate data in the submillimeter range.

6. Conclusion

The potential of the synthetic aperture method in combination with the recording of Fourier holograms has been demonstrated. It is a versatile tool that offers new applications for the investigation of microscopic (Fig. 4) and macroscopic objects (Fig. 5). Good results have been obtained for the intensity reconstruction and the double-exposure phase map, which was proven by an increase of the SNR value. The requirement of a flat sensor in order to carry out double-exposure measurement or any phase measurement utilizing the synthetic aperture method was pointed out. The misalignment problem due to the highly sensitive phase in double-exposure holography can be overcome by using the spatial averaging approach. It was found that the more laterally

displaced the holograms used for spatial averaging approach the better is the image quality. Furthermore, it was found that the image quality increases in a logarithmical manner with the number of adjacent holograms used. The resolution improvement experiment was carried out on the USAF 1951 test target. It was demonstrated that the SBP obtained is to the author's knowledge the largest reported SBP by means of digital holography. The highly detailed resolution was combined with a long DOF by using the EDOF method. It is to the author's knowledge the first time that the synthetic aperture method and the EDOF method have been combined in digital holography to produce firstly a reconstruction with all parts of the axial extended object in focus and secondly a three-dimensional topology map. A further improvement of the result can be obtained by a more homogeneous illumination (flat-top profile) and reflectivity of the object. All object points would then have the same impact on the recorded hologram. In that way the measurement accuracy could be increased. Suggested further developments include reducing the system components and decreasing vibration sensitivity utilizing fiber optics in conjunction with a pulsed coherent light source.

References

1. F. Le Clerc and M. Gross, "Synthetic-aperture experiment in the visible with on-axis digital heterodyne holography," Opt. Lett. **26**, 1550–1552 (2001).
2. F. Le Clerc and L. Collet, "Numerical heterodyne holography with two-dimensional photodetector array," Opt. Lett. **25**, 716–718 (2000).
3. J. Di, J. Zhao, H. Jiang, P. Zhang, Q. Fan, and W. Sun, "High resolution digital holographic microscopy with a wide field of view based on a synthetic aperature technique and use of linear CCD scanning," Appl. Opt. **47**, 5654–5659 (2008).
4. S. Zhang, "Application of super-resolution image reconstruction to digital holography," EURASIP J. Appl. Signal Process. **2006**, 1–7 (2005).
5. T. Baumbach, E. Kolenovic, V. Kebbel, and W. Jüptner, "Improvement of accuracy in digital holography by use of multiple holograms," Appl. Opt. **45**, 6077–6085 (2006).
6. J. H. Massig, "Digital off-axis holography with a synthetic aperture," Opt. Lett. **27**, 2179–2181 (2002).
7. T. Nakatsuji and K. Matsushima, "Free-viewpoint images captured using phase-shifting synthetic aperture digital holography," Appl. Opt. **47**, D136–D143 (2008).
8. L. Martinez-Len and B. Javidi, "Improved resolution synthetic aperture holographic imaging," Proc. SPIE **6778**, 7 (2007).
9. T. Kreis and K. Schlüter, "Resolution enhancement by aperture synthesis in digital holography," Opt. Eng. **46**, 0558031 (2007).
10. F. Gyímesi, Z. Füzessy, V. Borbély, B. Ráczkevi, A. Tibor Nagy, G. Molnárka, A. Lotfi, G. Molnár, A. Czitrovszky, A. Nagy, I. Harmati, and D. Szigethy, "Half-magnitude extensions of resolution and field of view in digital holography by scanning and magnification," Appl. Opt. **48**, 6026–6034 (2009).
11. L., Xu, Z. Guo, X. Peng, J. Miao, and A. Asundi, "Imaging analysis of digital holography," Opt. Express **13**, 2444–2552 (2005).
12. U. Schnars and W. Jueptner, *Digital Holography* (Springer, 2005).
13. J. W. Goodman, *Introduction to Fourier Optics*, 2nd ed. (McGraw-Hill, 1996).
14. W. S. Haddad, D. Cullen, J. C. Solem, J. W. Longworth, A. McPherson, K. Boyer, and C. K. Rhodes, "Fourier transform holographic microscope," Appl. Opt. **31**, 4973–4978 (1992).
15. A. W. Lohmann and S. Sinzinger, *Optical Information Processing* (Universitätsverlag, 2006).
16. S. W. Smith, *The Scientist and Engineer's Guide to Digital Signal Processing* (California Technical Publications, 2002).
17. T. Kreis, *Handbook of Holographic Interferometry: Optical and Digital Methods* (Wiley-VCH, 2005).
18. C. M. Do and B. Javidi, "Multi-focus holographic 3D image fusion independent component analysis," Proc. SPIE 6778, 67789P (2007).
19. C. P. McElhinney, B. M. Hennely, and T. J. Naughton, "Extended focused imaging for digital holograms of macroscopic three-dimensional objects," Appl. Opt. **47**, D71–D78 (2008).
20. M. L. Tachiki, M. Itoh, and T. Yatagai, "Simultaneous depth determination of multiple objects by focus analysis in digital holography," Appl. Opt. **47**, D144–D153 (2008).
21. H. Chang, T. Shih, N. Chen, and N. WenPu, "A microscope system based on bevel-axial method auto-focus," Opt. Lasers Eng. **47**, 547–551 (2009).